Synthesis of Ceria–Zirconia Nanocrystals with Improved Microstructural Homogeneity and Oxygen Storage Capacity by Hydrolytic Sol–Gel Process in Coordinating Environment

Mauro Epifani, Teresa Andreu, Sara Abdollahzadeh-Ghom, Jordi Arbiol, and Joan R. Morante*

Ceria–zirconia solid solution nanocrystals, $(1-x)CeO_2$–$xZrO_2$, $0 \le x \le 1$, are prepared by sol–gel processing in dodecylamine of solutions obtained by forced hydrolysis of inorganic salts. The as-prepared nanoparticles have a ceria cubic structure, up to $x = 0.35$, or are amorphous. Heat-treatment is carried out at temperatures ranging from 500 to 800 °C, the latter temperature begin suitable to obtain solid solutions throughout the composition range. For all the heating temperatures and x values, the fluorite cubic structure of pure CeO_2 transforms to a mixture (c') of the cubic c and tetragonal t'' phases for $x = 0.35$, and to tetragonal t phase only for $x = 0.8$ at 650 °C, $x = 0.65$ at 800 °C, and, to a very limited extent, $x = 0.5$ at 1000 °C. No evidence is obtained at low x values of the t phase, which is detrimental to the oxygen storage capacity. Prolonged heating at 1000 °C demonstrates that only for $x = 0.65$ a limited separation of CeO_2-rich nanocrystals occurs. The samples undergo the same transition without simultaneous occurrence of different phases, apart for the two mentioned limited cases. This result is attributed to the intimate mixing of the metal cations even in the early stages of processing. In as-prepared samples the Zr distribution becomes inhomogeneous when going from $x = 0.2$ to $x = 0.35$, but no early phase separations appear. The oxygen storage capacity is favorably influenced by the persistence of the cubic c' phase.

1. Introduction

Cerium dioxide (CeO_2) is widely used in three-way catalysis (TWC)[1] due to its ability to store oxygen in an oxygen-rich environment while releasing it in reducing conditions, according to the reaction

$$CeO_2 \underset{H_2O/CO_2}{\overset{H_2/CO}{\longleftrightarrow}} CeO_{2-x}$$

This property allows, under proper conditions, the simultaneous elimination of CO, NO_x, and hydrocarbons contained in automotive exhaust gases. The increasingly demanding limitations on automotive emissions have imposed harsher working conditions for TWCs, and the thermal stability of the catalyst has become a critical issue. In fact, ceria is known to undergo substantial sintering when cycled under the usual operating conditions of TWC.[2] This results in loss of the oxygen storage capacity (OSC), even though it has been pointed out that the phenomena underlying the decreased performance are not simply related to the surface area.[3] For this reason, the current TWCs are based on ceria–zirconia solid solutions.[4] With respect to pure ceria, the solutions display superior thermal stability and OSC, even when the surface area is decreased by the operating conditions. The CeO_2–ZrO_2 solid solutions have more complex phase diagrams than pure CeO_2. The large cation size difference (0.084 nm for Zr^{4+} against 0.097 for Ce^{4+}) reduces the solubility range within which the cubic c phase is stable, and introduces additional metastable phases.[5] The Zr concentration must be tuned in order to control the phase composition of the system: preserving the cubic c phase is beneficial for the OSC, while the appearance of the tetragonal t phase is detrimental. Moreover, homogeneous materials are preferred to phase-segregated ones, since it is believed that this results in better stability and redox properties.[4b]

The grain size of the material plays an important role in the phase transformations of the solid solutions, and it has been shown that the pseudocubic phase (c'), which is beneficial for the OSC, is stable over a broad composition range for grain size

Dr. M. Epifani
Consiglio Nazionale delle Ricerche – Istituto per la Microelettronica e Microsistemi (C.N.R.-I.M.M.), via Monteroni, I-73100 Lecce, Italy
E-mail: mauro.epifani@le.imm.cnr.it
Dr. T. Andreu, Prof. J. R. Morante
Catalonia Institute for Energy Research
IREC c/Jardins de les Dones de Negre 1, 08930-Sant Adria del Besos, Barcelona, Spain
S. Abdollahzadeh-Ghom, Prof. J. R. Morante
M2E-IN2UB-XaRMAE
Departament d'Electrònica
Universitat de Barcelona
C. Martí i Franquès 1, 08028 Barcelona, CAT, Spain
Prof. J. Arbiol
Institucio Catalana de Recerca i Estudis Avançats
ICREA and Institut de Ciència de Materials de Barcelona
ICMAB-CSIC, 08193 Bellaterra, CAT, Spain

DOI: 10.1002/adfm.201200380

below 30 nm.[6] Moreover, the grain size influences the defect formation energy, and in particular the concentration of oxygen vacancies. Also, it is known that the grain boundary impedance and the electronic conductivity increase in nanocrystalline ceria.[7] All these factors can influence the overall conduction mechanisms and the related OSC.

Preparing ceria–zirconia solid solutions with controlled phase in the nanosized regime is therefore of strong interest for improved OSC. The availability of solid solutions with extended stability of the cubic phase would allow a broader choice of compositions, according to the particular operating conditions. In particular, it would be possible to choose the desired Zr concentration, while at the same time retaining the correct phase composition. For these reasons an intensive research effort has been devoted to the synthesis of nanocrystalline ceria–zirconia solid solutions. Preparation procedures include solid-state synthesis,[8] high-energy milling,[9] hydro/solvothermal synthesis,[10] co-precipitation,[11] the citrate method,[12] inverse micelles,[13] and mesoporous templates.[14]

In recent works,[15] we have been developing a synthesis of metal oxide nanocrystals based on sol–gel processing in a hot coordinating amine environment. In the process, a metal oxide precursor is prepared by forced hydrolysis of inorganic salts, and is then injected into hot amine. The formation process is very fast, and results in isolated nanoparticles. This feature could be very useful for preparing phase homogeneous multicomponent systems. The underlying concept is that due to the kinetics of the process, the initial solution homogeneity can be "frozen" up to the nanocrystal formation stage. Further heat-treatment would result in nanocrystal growth and redistribution of the metal cations without *starting* segregation regions. We have successfully applied this approach to the synthesis of metal ferrites.[15d] Attracted by the importance of the ceria–zirconia system, our aim in this work was to investigate the suitability of the process to prepare such solid solutions with improved phase homogeneity. The final result was the synthesis of materials without the formation of the undesired *t* phase at low *x* (Zr concentration) values. This result is also attributed to the control of the nanocrystal size in the nanometer range, another important feature of the process. More importantly, the phase evolution occurred without the simultaneous presence of different phases: all the nanocrystals underwent the same phase transformation at the same time. The improved phase homogeneity is also crucial for the OSC performance. Hence, the OSC was increased by two orders of magnitude by addition of 20% Zr with respect to pure ceria, and was practically constant throughout the 0.2–0.5 range for *x*.

2. Results

The phase composition has a crucial impact on the catalytic performances of CeO_2–ZrO_2 solid solutions. Thus, the first section will be devoted to the combined use of XRD and Raman spectroscopy for elucidating the structural features of the samples. It will be shown that there is a continuous transition from the fluorite cubic structure of pure CeO_2, through the incorporation of increasing concentrations of ZrO_2, to the tetragonal phase of pure ZrO_2. This transition occurs through the additional appearance of only the *t*″ tetragonal phase, up to $x = 0.8$ or 0.65, depending on the heating temperature. Finally, the results of the oxygen storage properties measurements will be presented.

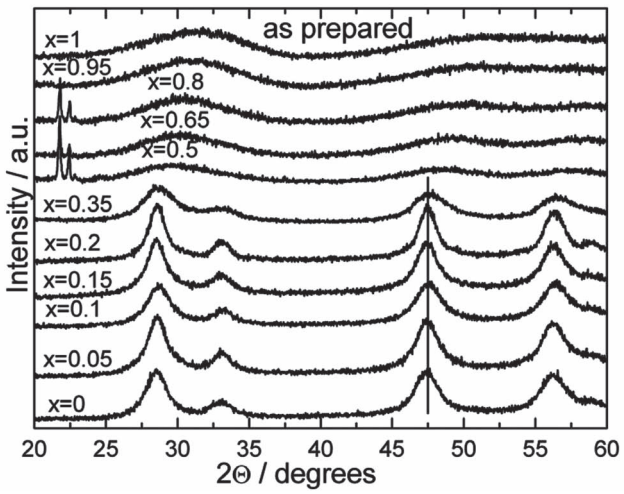

Figure 1. XRD patterns of the as-prepared $(1–x)CeO_2$–$xZrO_2$ samples. The vertical line is only a guide for the eye.

2.1. The Cubic Phase Throughout the Composition Range: XRD and Raman Analysis of Low Temperature Samples

Recalling that *x* is the Zr concentration, in the phase diagram of the CeO_2–ZrO_2 ($(1–x)CeO_2$–$xZrO_2$) system,[5a] for $x = 0$ pure CeO_2 crystallizes in the fluorite (cubic) structure. A cubic structure, denoted by *c*, is generally reported up to $x = 0.15$. Then, two tetragonal metastable phases, *t*′ and *t*″, have been identified and can be distinguished by the XRD patterns. The *t*″ phase is indistinguishable by XRD from the *c* phase; both constitute the *c*′ phase. The *t*″ and *c* phases can be distinguished by Raman spectroscopy. The metastability of the *t*′ and *t*″ phases results in conversion to the tetragonal *t* phase, which is reported at various *x* values, depending on the material synthesis, heat-treatment temperature, and other experimental conditions. For high *x* values, the *t* phase is obtained upon cooling and for $x > 0.95$ the monoclinic phase of zirconia is the stable one.

Figure 1 shows the XRD patterns of the as-prepared samples. For *x* up to 0.35, the pattern of pure, cubic CeO_2 was observed, with no appreciable peak shift indicating Zr incorporation. For higher *x* values, the samples appeared very poorly crystallized. ZrO_2 crystallization is kinetically hindered at low processing temperatures, so when it becomes the prevailing component the overall material crystallization is also prevented. On the other hand, there were no peaks of cubic ceria, indicating the absence of early phase separations between the two components of the solid solution. The peaks at $2\theta < 25°$ for $0.5 \leq x \leq 0.8$ were not identified and could be due to reprecipitation of byproducts. To favor the formation of the solid solution, the as-prepared samples were heat-treated at 500 °C. In **Figure 2** the related patterns are shown for *x* up to 0.2. Shift of the cubic fluorite peaks occurred with respect to $x = 0$. As discussed below, the analysis of the cell parameters showed

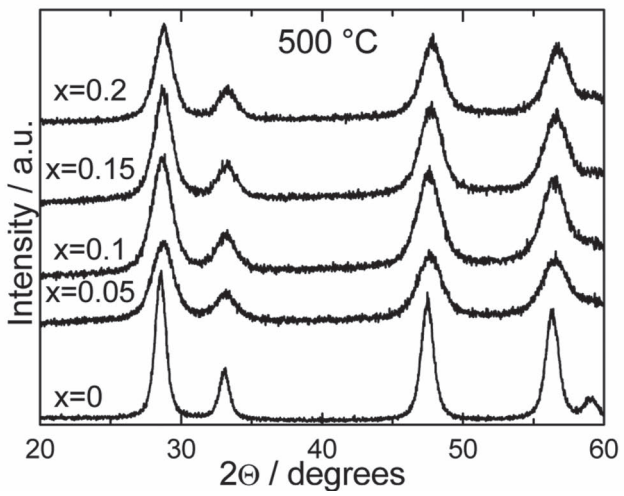

Figure 2. XRD patterns of the $(1–x)CeO_2–xZrO_2$ samples heat-treated at 500 °C.

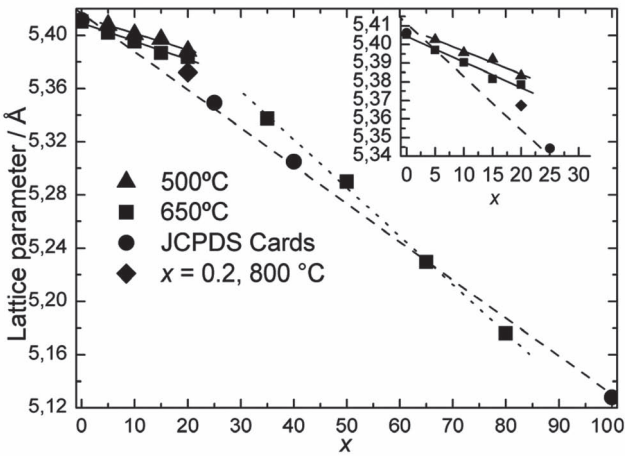

Figure 4. Comparison between the experimental cubic lattice parameter for various heating temperatures and the theoretical dashed line based on the JCPDS cards. The inset shows the enlargement of the low x region.

a linear dependence on x, as expected upon formation of the solid solution, but the values were still far from the theoretical line. For this reason, heat-treatments of samples with higher x value were skipped and the whole series was heat-treated at 650 °C. The XRD patterns are shown in **Figure 3**. The peak shift was more evident than for the 500 °C series. The lattice parameter was obtained by Rietveld analysis of the patterns and the results are reported in **Figure 4**. As reference, an ideal line was calculated by using existing JCPDS cards[16] and considering a Vegard's law dependence of the cell parameter on the x value. It has been pointed out[5] that nanocrystalline species display remarkable lattice expansion with respect to bulk samples, resulting in deviation from ideal behavior. Nevertheless, comparison with a theoretical line is still useful for evaluating the relative changes between sample series. Up to Zr concentration $x = 0.35$, it can be seen that after heat-treatment at 650 °C the cell parameter approaches the theoretical line more than for

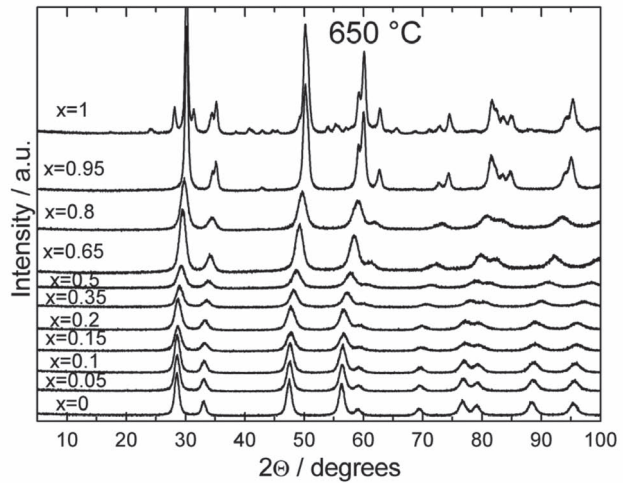

Figure 3. XRD patterns of the $(1–x)CeO_2–xZrO_2$ samples heat-treated at 650 °C.

500 °C. For $0.1 \leq x \leq 0.2$ the cell parameter is still larger than the theoretical value. A sample with $x = 0.2$ was heat-treated at 800 °C. The related lattice parameter, also shown in Figure 4, was much closer to the theoretical line. It was concluded that the Zr incorporation for $x \leq 0.2$ was a kinetic issue, requiring higher heat-treatment temperatures. On the other hand, for $0.35 \leq x \leq 0.8$ the lattice parameter was much closer to the theoretical line than for smaller Zr concentrations.

As concerns the phase identification, first of all throughout this work the t' phase, which can be identified by the splitting of the (400) and (004) XRD peaks, was never observed. The XRD patterns in Figure 3 were assigned to the cubic phase (c or c') up to at least $x = 0.65$. For higher x values, peak broadening made the phase identification ambiguous; it was clarified by the Raman data. For $x = 0.95$ the pattern was indexed to the tetragonal t phase, while for pure zirconia the monoclinic m phase was also present (Figure 3). The stabilization of tetragonal zirconia up to $x = 0.95$ instead of the monoclinic phase has been attributed to the presence of ceria.[17]

Figure 5 shows the room-temperature Raman spectra of as-prepared samples. A single peak is observed at about 460 cm^{-1} for $x = 0$, as expected for the cubic structure of ceria.[18] Band asymmetry has been interpreted as a size effect.[19] A shoulder at 610 cm^{-1} was also observed up to $x = 0.2$, attributed to oxygen vacancies.[20] For $x > 0.35$, the Raman spectra indicate the amorphous nature of the samples, in agreement with the XRD results. **Figure 6** shows the Raman spectra of the samples heat-treated at 650 °C. A new band appears at 290 cm^{-1} for $x = 0.35$ and shifts to 310 cm^{-1} for $x = 0.5$. In the Raman spectra of the t, t' and t'' phases, six bands are allowed.[5a,6] The first two bands, below 250 cm^{-1}, disappear when the Zr concentration is progressively lowered, so the 307 cm^{-1} band can be used for determining the minimum Zr concentration for which the t'' phase appears.[6] In Figure 6 this threshold is $x = 0.35$. Moreover, a strong 464 cm^{-1} peak coupled with a weak 307 cm^{-1} peak indicates the presence of the c component[6] (in the following, these bands will be denoted with these wavenumber values as a

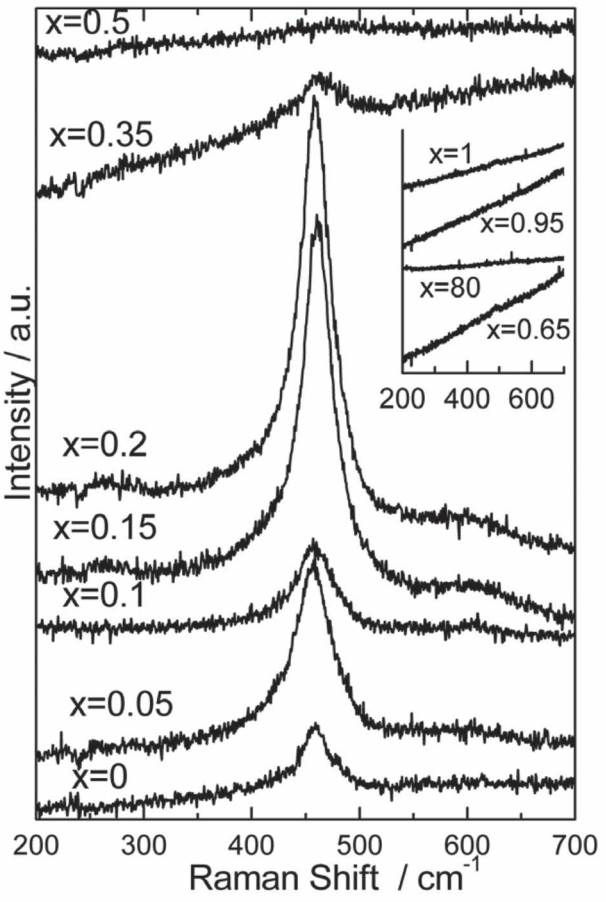

Figure 5. Raman spectra of the as-prepared $(1–x)CeO_2–xZrO_2$ samples.

reference, despite the exact position changes according to the sample composition). Hence, from the observation of Figure 6 we conclude that the c' phase ($c + t''$) is present up to x = 0.65, even though at such Zr concentration the t'' is expected to be largely prevalent. At x = 0.8 the tetragonal t phase is formed, also shown by the strong band at about 650 cm^{-1}. A weaker and broader signal in the same position for x = 0.65 showed the onset of the tetragonal distortion. This interpretation clarified the XRD results of Figure 3. Finally, the spectrum for x = 1 is markedly different, in agreement with the formation of monoclinic zirconia observed in XRD. The XRD patterns do not show simultaneous presence of the c' and t phases, which would be indicated by the appearance of new peaks. This result was not surprising at as low as 650 °C heating temperature, but in the following we will see that this phase homogeneity of the system was kept over a much broader range of conditions.

2.2. XRD and Raman Analysis of High Temperature Samples

The next question is the stability of the solid solutions at higher heating temperatures. For these reasons, selected samples, with x spanning the range where phase separations could be more likely, were heat-treated at 800 °C for 1 h and at 1000 °C for 5 h. The latter samples were prepared following a criterion recently[5b] presented to assess phase homogeneity.

Figure 7A shows the XRD patterns of the 800 °C series. At x = 0.65 the t phase was indicated by the weak (102) reflection at about 42°. In the 650 °C series, this peak clearly occurred only at x = 0.95. An evident peak shift indicated the Zr incorporation in the cubic lattice, and a slight peak narrowing with respect to Figure 3 indicated a limited grain growth. Figure 7B, related to the 1000 °C series, shows at x = 0.5 a deformation of the XRD peaks, in the position marked with the asterisks. Deconvolution of the peaks (see the Supporting Information, Figure S1) showed that they could be interpreted as the reflections of the t phase. The other peaks of the t phase were completely overlapped with those of the c' phase, which was still prevailing. For x = 0.65, similar peak distortion was observed, but peak deconvolution (Supporting Information, Figure S2) shows the presence of an additional component, in a position very similar to that of ceria-rich materials. Correspondingly, the lowest angle peak is also asymmetrical and shows an additional component, again corresponding to the reflection of ceria-rich materials. The phase composition was further investigated by Raman spectroscopy. The results are shown in **Figure 8**. The t'' phase appears at x = 0.35 (band at 307 cm^{-1}); the c' phase is present up to x = 0.65 for both 800 and 1000 °C treatments. The question whether at x = 0.65 and 800 °C a phase mixture is present will be discussed in detail in the following. The Raman spectrum for the x = 0.65 sample at 1000 °C shows a strongly

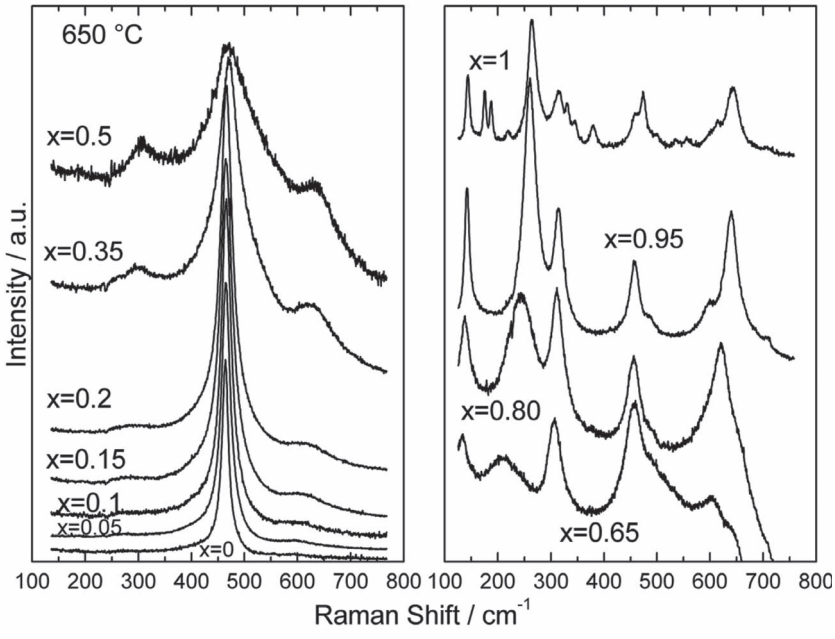

Figure 6. Raman spectra of the $(1–x)CeO_2–xZrO_2$ samples heat-treated at 650 °C.

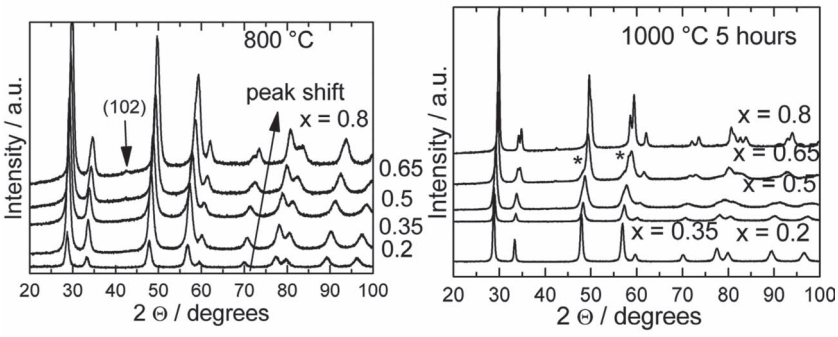

Figure 7. XRD patterns of the $(1-x)CeO_2$–$xZrO_2$ samples heat-treated at 800 and 1000 °C. The stars in the 1000 °C patterns indicate additional peaks with respect to the cubic/tetragonal peaks.

distorted 464 cm^{-1} band, with a lower energy component that can be clearly related to the ceria-rich nanoparticles evidenced in the XRD data.

The lattice parameter was calculated by Rietveld refinement, and the results are shown in **Figure 9**, which is an update of Figure 4. It is clear that, for $x = 0.2$, where after 800 °C the Zr incorporation was still not complete, the 1000 °C treatment induces an even better approximation of the theoretical lattice value. For higher x values, heat-treatment up to 1000 °C does not result in obvious changes with respect to 650 or 800 °C. More importantly, the lattice parameter data replotted in detail for each heating temperature (Figure S3 in the Supporting Information) are clearly fitted by a straight line, following the Vegard's law and showing the effective Zr incorporation.

It has been evidenced that limiting the grain growth favors the persistence of metastable phases in ceria-zirconia solid solutions.[6] In the nanometer range, the surface contribution to the Gibbs free energy of the system becomes particularly important and can give rise to stability inversion phenomena in the phase diagram.[21] Thus we calculated the grain size trend in our samples depending on the heating temperature, in order to gain some insight into the phase stability in our samples. The results are shown in **Figure 10**. Heat-treatments at 800 °C increased the size just above 10 nm for all the samples, from a value ranging about 7–8 nm at 650 °C. Moreover, the size was practically independent on the Zr content. When the samples were heat-treated at 1000 °C, the size still remained well below 30 nm. For 1000 °C heating, the size increase with respect to lower temperatures is evident, and the curve has a minimum just at $x = 0.5$.

2.3. Structural and Compositional Investigation of the Solid Solutions by TEM

Structural investigation at the nanoscale was carried out by TEM, for a close assessment of the nanocrystals size and structure, and for getting a deeper insight about the trends of the Zr incorporation behavior. Samples with $x = 0.20$ and 0.35 were investigated, since in that range the incorporation shows a different trend (see Figure 4). As-prepared samples were investigated since the initial Zr distribution is crucial in determining the following structural evolution. **Figure 11** shows the results of the TEM studies on the as-prepared sample with $x = 0.35$. The general view clearly shows the presence of discrete, faceted nanocrystals, whose mean size was 3.2 ± 0.7 nm. A mean size of 4.3 ± 1.0 nm was found for $x = 0.2$. The HRTEM observation of the nanocrystals, like that in inset, shows crystallization in the CeO_2 cubic phase, according to the related FFT analysis in the other inset. Another power spectra analysis example is shown in the Supporting Information (Figure S4). For every spot, the comparison between the obtained experimental results and the calculated atomic plane distances shows a very good agreement with the cubic CeO_2 structure. No evidence of additional phases was obtained. Similar results were obtained for the sample with $x = 0.2$, and they are shown in the Supporting Information (Figure S5). The distribution of the Zr cations was investigated by means of electron energy loss spectroscopy (EELS). In this way, energy-filtered TEM (EFTEM) elemental mappings of the samples were obtained, like that reported in the Supporting Information (Figure S6) for the sample with $x = 0.2$. The results were different for the two samples. For $x = 0.2$ EFTEM analysis obtained over some nanoparticles showed an homogeneous distribution of Zr on the CeO_2 nanoparticles,

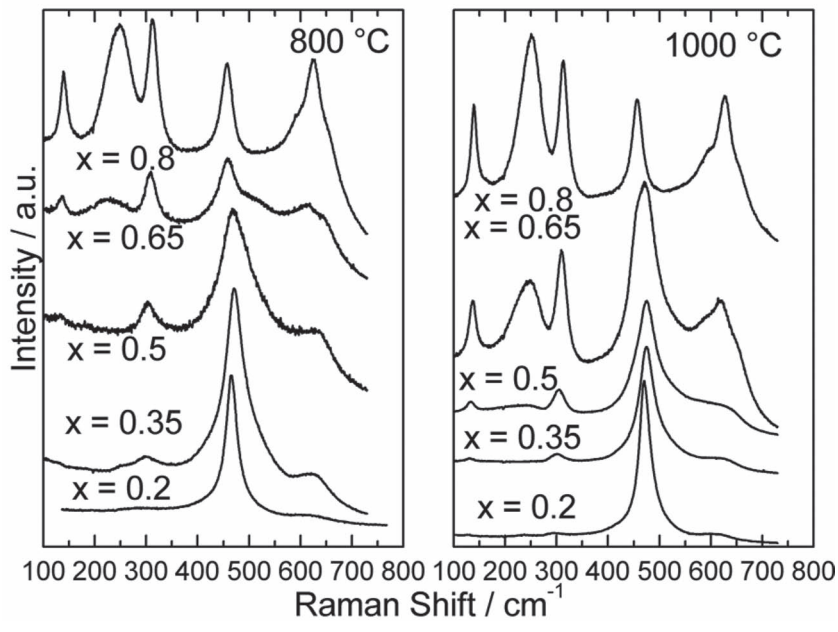

Figure 8. Raman spectra of the $(1-x)CeO_2$–$xZrO_2$ samples heat-treated at 800 and 1000 °C.

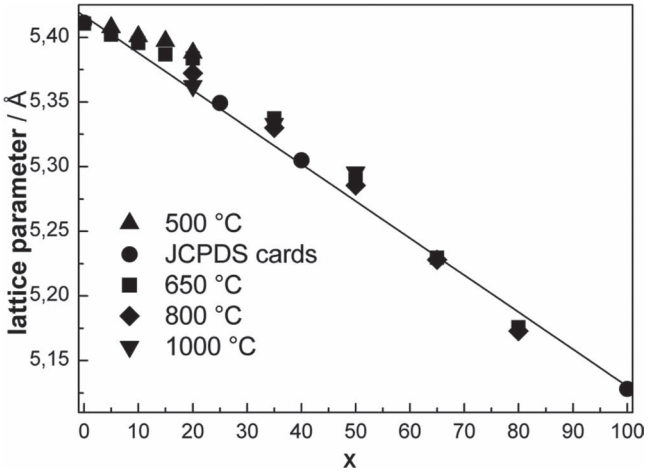

Figure 9. Comparison between the experimental cubic lattice parameter for heating temperatures from 500 to 1000 °C and the theoretical line based on the JCPDS cards.

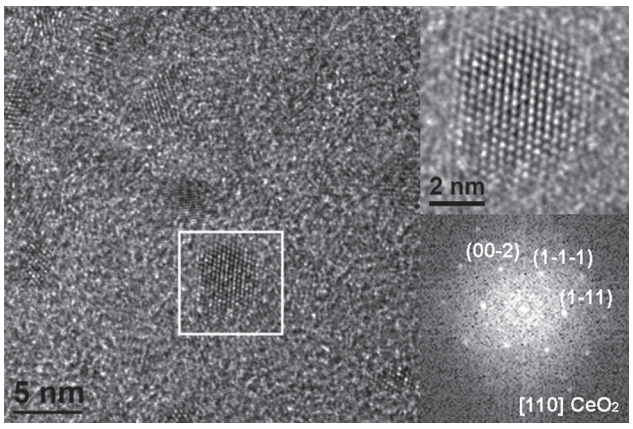

Figure 11. General view, high-resolution image of the marked area, and related FFT spectrum of as prepared sample with $x = 0.35$.

with a relative percentage of the two elements very close to the expected value: 80.12% for Ce and 19.88% for Zr. The situation was different for $x = 0.35$, where Zr depletion regions were observed, with atomic concentrations as 92.51% for Ce and 7.49% for Zr in some regions, while in other points the relative concentrations were close to the nominal value. It is clear that with increasing Zr concentration the product formation pathways are different. Even visually, the as-prepared sample with $x = 0.35$ had a gelatinous and voluminous appearance, different to the sample with $x = 0.2$. With increasing Zr concentration, the products more and more resemble an amorphous gel (as shown by XRD and Raman spectra of as-prepared materials, Figure 1 and 5) while for low x they are constituted by ceria nanocrystals within which Zr species are dispersed. In the latter case, diffusion of Zr cations in the already formed ceria nanocrystals is necessary to get the solid solution. For high x, structural reorganization of a softer material is necessary. From the experimental results, the latter process seems more favorable, but at this stage, a careful explanation of the formation mechanism of the solid solutions cannot be provided.

2.4. Oxygen Storage Properties of the Ceria–Zirconia Solid Solutions

The basic thermal analysis for measuring the OSC properties is shown in the Supporting Information (Figure S7). The related curves for selected samples, up to $x = 0.5$, are shown in **Figure 12**. From these curves, the OSC data were obtained as described in the Experimental Section; they are reported in **Figure 13**. The OSC value steeply increases for small increases of the x value, and reaches a maximum for $x = 0.2$, where it increases by about two orders of magnitude if compared with pure ceria, where it was negligible. The large increase of the OSC with increasing x is a confirmation of the successful Zr incorporation. For $x \geq 0.2$, the OSC remains practically constant up to $x = 0.5$.

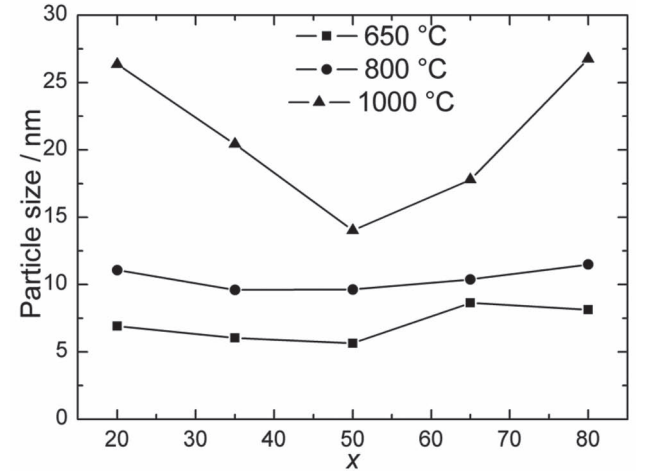

Figure 10. Particle size of the $(1–x)CeO_2–xZrO_2$ samples heat-treated from 650 to 1000 °C.

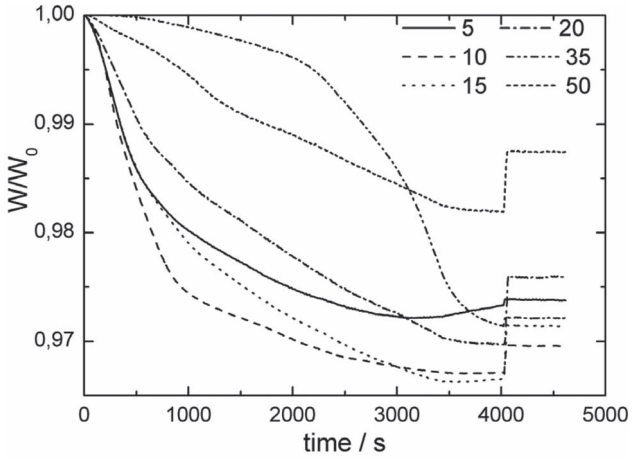

Figure 12. TG curves for the $(1–x)CeO_2–xZrO_2$ samples heat-treated at 650 °C.

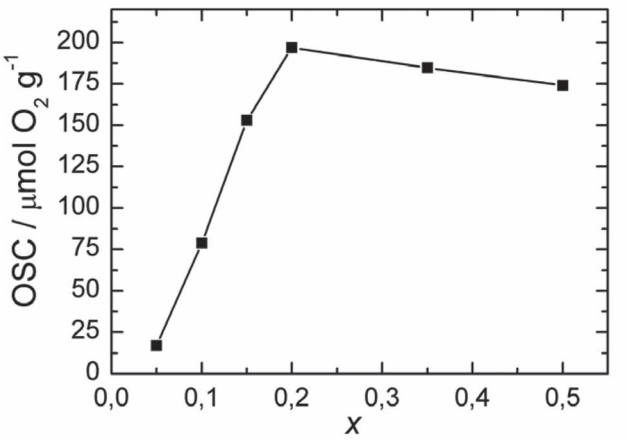

Figure 13. OSC as a function of x for the $(1-x)CeO_2$–$xZrO_2$ samples heat-treated at 650 °C.

3. Discussion

Upon cooling the ceria–zirconia solid solutions, the t' and t'' phases are expected below 1200 °C and for $x > 0.2$. Similarly to Zhang et al.,[6] we never observed the t' phase in our work. The t' phase is formed from the t'' phase through a diffusionless transition, which then requires extra driving energy, given for instance by high stress concentration. While such conditions can be found in solid-state synthesized samples, like in the work by Yashima et al.,[5a] it has been shown that solution-prepared nanocrystals, with limited sintering, suffer much less stress during the structural evolution. The t phase in Yashima's phase diagram[5a] existed above 1200 °C and for high x. We could identify the t phase at lower temperature and above all for x values decreasing from 0.8 (650 °C) to 0.65 (800 °C) to 0.5 (1000 °C). This result is in agreement with the findings of Zhang et al.[6] Instead, a novel feature of the present work is the homogeneous phase transformation of the materials. For instance, Zhang et al. observed the coexistence of t and c' phases at 800 °C for $x = 0.7$, and for lower x at 1200 °C. In our work we observe a single phase after heating at 650 and 800 °C (we recall that the c and t'' are considered a single cubic phase). First the c' forms from the c phase at $x = 0.35$, then the t phase appears at the just-mentioned x values. At 800 °C, the (102) tetragonal t peak in the XRD pattern for $x = 0.65$ posed an interpretation problem. Since it is intrinsically very weak, its presence suggests that the tetragonal component in the sample should be very high. This is also shown by the deconvolution of the XRD patterns shown in the Supporting Information (Figure S8). On the other hand, the Raman spectra in Figure 8 showed an intensity ratio between the 467 and 307 cm^{-1} bands that should be still characteristic of the c' phase. Reasoning on this point stimulated a more complex view of the phase transformations in our samples. We deconvoluted (Supporting Information, Figure S9) the Raman spectra of 650 °C samples, for x ranging from 0.2 to 0.5. With increasing x, the 467 cm^{-1} band is more and more asymmetric with the inclusion of new components. This trend shows an increasing distortion of the purely cubic structure. It is then necessary to view the samples as composed of nanocrystals with a distribution of lattice distortions with respect to the cubic structure. This set of variously distorted nanocrystals evolves homogeneously (continuous Gibbs free energy throughout the sample) toward the following phase transition. Hence the description in terms of c' or t phases becomes schematic and the actual situation is only given by a crossed use of XRD and Raman data. In particular, at 800 °C and $x = 0.65$, the Raman spectra indicate that a set of lattice distortions from the initial cubic symmetry toward the final tetragonal structure is present.

Di Monte and Kaspar[5b] pointed out the importance of the favorable initial distribution the Ce and Zr cations for preparing homogeneous ceria–zirconia solid solutions. In previous work,[15d] we have pointed out the importance of avoiding metal cations segregation in the initial stage of the material formation, when preparing solid solutions. From the analysis of the TEM results, we have seen that separate nanocrystals of CeO_2 or ZrO_2 were never formed, even for high Zr content where the cation distribution was less homogeneous. This initial distribution of the two cations, together with the small size of the nanocrystals, helps in stabilizing the distorted structures against early phase separations. Only after prolonged heating at 1000 °C, for $x = 0.5$ and 0.65 limited inhomogeneities occurred, probably favored by the size growth or by the composition. In the first case, XRD peak deconvolution showed the simultaneous occurrence of t and c' phases. For $x = 0.65$, a small amount of ceria-rich nanocrystal segregated.

For evaluating the OSC of the samples, we focused on the 650 °C series, where Zr incorporation was not complete, in order to set the most demanding test conditions and to evidence the performance differences between the samples. For the same reason, the samples were pre-conditioned in nitrogen instead of a reducing mixture with hydrogen. As expected, successful inclusion of Zr boosted the OSC performance of the solid solutions, with a sharp increase when going to $x = 0.2$. Then, the OSC was practically constant up to $x = 0.5$. This was the most important result of these tests. One of the most important features for the OSC performance is the homogeneity of the material. The lack of phase separations and, above all, the homogeneous phase transformations ensured this condition. Hence, even in the low temperature series, a very stable OSC performance was obtained. An influence of the surface area was excluded, since it ranged about 90–95 $m^2\ g^{-1}$ for the solid solutions, with respect to a value of about 80 $m^2\ g^{-1}$ for pure CeO_2 and ZrO_2 (see the Supporting Information).

4. Conclusions

Effective formation of ceria–zirconia solid solution was obtained throughout the Zr concentration range after heat-treatment at 800 °C. The solution synthesis of the initial nanoparticles avoided the formation of the t' metastable phase throughout the composition and temperature range. The t phase was found after cooling the samples at a decreasing x value, with increasing the heating temperature. These results were in agreement with the nanometric size range of the samples, which was always below 30 nm, even after heating at 1000 °C. Remarkably, the phase transformations homogeneously affected the whole sample,

without simultaneous occurrence of different phases. Only for $x = 0.5$ and 0.65, after heating at 1000 °C, coexistence of different crystallographic phases or phase separation occurred, but to a very limited extent. This result was explained on the following basis: i) the precursor mixing at the molecular scale in the starting solutions, and the fast nanocrystal formation kinetics, avoiding early phase separations; and, ii) the nanocrystal size below 10 nm up to heat-treatment at 800 °C, and below 30 nm 1000 °C. The phase homogeneity beneficially affected the OSC property, which was enhanced by Zr addition at $x = 0.2$ and was above all constant up to $x = 0.5$.

5. Experimental Section

Starting Solutions: a) Single oxides. CeO_2 solutions were prepared by dissolving $Ce(NO_3)_3{\cdot}6H_2O$ (2.6 mmol) in methanol (10 mL), then adding acetylacetone (acacH), with an acacH/Ce molar ratio of 3:1. After 1 h from the addition of acacH, a 30 wt-% ammonia solution in water was dropped, followed by vigorous stirring for further 24 h. The NH_3/Ce molar ratio was 0.6:1. For preparing the ZrO_2 sol, anhydrous $ZrCl_4$ (3.9 mmol) were reacted with of methanol (10 mL) in a glove-box, with evolution of heat and vapors. After 1 h from methanol addition, water was added, with a H_2O/Zr molar ratio ranging from 16:1 to 64:1.

b) Solid solutions. The composition of the solid solutions will be indicated by the x value in the general formula $(1–x)CeO_2–xZrO_2$. For any x value between 0 and 1, the required amounts of $Ce(NO_3)_3{\cdot}6H_2O$ and $ZrCl_4$ were weighed in a glove-box, mixed and dissolved in MeOH (10 mL). For $0 < x \leq 0.5$, a fixed amount of $Ce(NO_3)_3{\cdot}6H_2O$ (3.6 mmol) was used, while for $0.5 < x < 1$, a fixed amount of anhydrous $ZrCl_4$ (3.9 mmol) was kept. For all x values, after dissolution of the precursors, acetylacetone (acacH) was added, with an acacH/Ce molar ratio of 3:1. For $0 < x \leq 0.5$, after 15 min 30 wt-% ammonia solution in water (100 µL) was added. For $0.5 < x < 1$, after adding acetylacetone, water was added dropwise, with a H_2O/Zr molar ratio ranging from 16:1 to 64:1. Finally, ammonia solution was added with the same NH_3/Ce molar ratio used for $0 < x \leq 0.5$.

Processing of the Starting Solutions: In a 500 mL flask, thoroughly degassed with nitrogen, *n*-dodecylamine (10 mL) was heated up to 160 °C, then the selected starting solution (2 mL) was injected in the flask through a septum. The solution temperature dropped to about 90 °C and was maintained constant by decreasing the power supply to the flask heater. After 2 h from the injection step, heating was stopped. Methanol was added to the reaction slurry, resulting in flocculation. The solid product was recovered by centrifugation, further washed with methanol and dried at 90 °C. White powders were obtained for pure zirconia, while they had an increasing yellow–brown color with decreasing x, and for pure ceria they were deep yellow. The as-prepared powders were crushed and heat-treated in a muffle furnace for 1 h at 500 or 650 °C, with a heating rate of 5 °C min^{-1}. The products were yellow for all x values, except for white pure ZrO_2.

Characterization: The crystallographic phase of the samples was determined by X-ray diffraction (XRD) with a Panalytical Alfa diffractometer using the Cu Kα1 radiation (λ = 1.5406 Å). The cell a parameter values were calculated by adjusting the profile using the Fullprof program,[22] taking into account a single phase with fluorite or pseudocubic symmetry.

The green line (λ = 514 nm) of a Jobin Yvon T64000 spectrometer with an INNOVA 300 Coherent Ar laser and a bidimensional CCD detector cooled with liquid nitrogen was used for Raman analysis of the solutions and powders.

The structural and morphological characterization of selected samples was carried out by means of transmission electron microscopy (TEM). In order to obtain the high-resolution TEM (HRTEM) results we used a field emission gun microscope Jeol 2010F, operated at 200 kV and with a point-to-point resolution of 0.19 nm. The software used for digital image analysis and crystallographic indexation was the Digital Micrograph (Gatan) and Carine, respectively. For EELS and EFTEM analyses we used a Gatan Image Filter (GIF2001). The samples for the TEM observations were prepared by placing a drop of nanocrystals suspensions in toluene onto a carbon coated copper grid, followed by drying.

Oxygen storage capacity was measured by thermogravimetric analysis (TG), using a thermobalance TGA-SDTA 851e/SF/1100 from Mettler Toledo. 15 mg of sample powder was heated up to 600 °C in nitrogen (50 mL min^{-1}) in order to release oxygen from the sample. After 10 min of stabilization, synthetic air was introduced resulting to an increase in sample weight due to the uptake of oxygen from air. This mass change is considered as OSC of the samples represented in µmol-O_2 g^{-1} catalyst, and is calculated as reported in the Supporting Information.

Supporting Information

Supporting Information is available from the Wiley Online Library or from the author.

Acknowledgements

Authors acknowledge CSIC/CNR project 2010IT0001 (SYNCAMON) and SOLAR project DM19447. This work was partially supported by the European Regional Development Funds European (ERDF, "FEDER Programa Competitivitat de Catalunya 2007-2013"), the Spanish Government projects Consolider Ingenio 2010 CSD2009 00013 IMAGINE, CSD2009 00050 MULTICAT and MICINN project NANO-EN-ESTO (ref. MAT2010-21510). JA acknowledges the funding from the Spanish MICINN project MAT2010-15138 (COPEON). The authors would like to thank the TEM facilities in Serveis Cientificotecnics from Universitat de Barcelona.

Received: February 7, 2012
Published online: April 13, 2012

[1] A. Trovarelli, M. Boaro, E. Rocchini, C. de Leitenburg, G. Dolcetti, *J. Alloys Compd.* **2001**, *323–324*, 584–591.
[2] V. Perrichon, A. Laachir, S. Abouarnadasse, O. Touret, G. Blanchard, *Appl. Catal. A* **1995**, *129*, 69–82.
[3] E. Mamontov, T. Egami, R. Brezny, M. Koranne, S. Tyagi, *J. Phys. Chem. B* **2000**, *104*, 11110–11116.
[4] a) J. Kašpar, P. Fornasiero, N. Hickey, *Catal. Today* **2003**, *77*, 419–449; b) J. Kašpar, P. Fornasiero, *J. Solid State Chem.* **2003**, *171*, 19–29.
[5] a) M. Yashima, H. Arashi, M. Kakihana, M. Yoshimura, *J. Am. Ceram. Soc.* **1994**, *77*, 1067–1071; b) R. Di Monte, J. Kašpar, *J. Mater. Chem.* **2005**, *15*, 633–648.
[6] F. Zhang, C.-H. Chen, J. C. Hanson, R. D. Robinson, I. P. Herman, S.-W. Chan, *J. Am. Ceram. Soc.* **2006**, *89*, 1028–1036.
[7] S. Basu, P. S. Devi, H. S. Maiti, *J. Mater. Res.* **2004**, *19*, 3162–3171.
[8] a) K. Eguchi, N. Akasaka, H. Mitsuyasu, Y. Nonaka, *Solid State Ionics* **2000**, *135*, 589–594; b) A. Varez, E. Garcia-Gonzalez, J. Sanz, *J. Mater. Chem.* **2006**, *16*, 4249–4256.
[9] a) A. Trovarelli, F. Zamar, J. Llorca, C. de Leitenburg, G. Dolcetti, J. T. Kiss, *J. Catal.* **1997**, *169*, 490–502; b) S. Enzo, R. Frattini, F. Delogu, A. Primavera, A. Trovarelli, *Nanostruct. Mater.* **1999**, *12*, 673–676.
[10] a) C. S. Wright, R. I. Walton, D. Thompsett, J. Fisher, S. E. Ashbrook, *Adv. Mater.* **2007**, *19*, 4500–4504; b) M. K. Devaraju, X. Liu, K. Yusuke, S. Yin, T. Sato, *Nanotechnology* **2009**, 405606/1–6; c) T. Taniguchi, T. Watanabe, N. Matsushita, M. Yoshimura, *Eur. J. Inorg. Chem.* **2009**, 2054–2057.

[11] a) C. E. Hori, H. Permana, K. Y. Simon Ng, A. Brenner, K. More, K. M. Rahmoeller, D. Belton, *Appl. Catal., B* **1998**, *16*, 105–117; b) T. Masui, K. Nakano, T. Ozaki, G.-Y. Adachi, Z. Kang, L. R. Eyring, *Chem. Mater.* **2001**, *13*, 1834–1840; c) C. Bozo, F. Gaillard, N. Guilhaume, *Appl. Catal., A* **2001**, *220*, 69–77; d) J. Ouyang, H. Yang, *J. Phys. Chem. C* **2009**, *113*, 6921–6928.

[12] J. Kaspar, P. Fornasiero, G. Balducci, R. Di Monte, N. Hickey, V. Sergo, *Inorg. Chim. Acta* **2003**, *349*, 217–226.

[13] Y. An, M. Shen, J. Wang, *J. Alloy. Compd.* **2007**, *441*, 305–310.

[14] S. Abdollahzadeh Ghom, C. Zamani, S. Nazarpour, T. Andreu, J. R. Morante, *Sens. Actuators, B* **2009**, *140*, 216–221.

[15] a) M. Epifani, R. Díaz, J. Arbiol, E. Comini, N. Sergent, T. Pagnier, P. Siciliano, G. Faglia, J. R. Morante, *Adv. Funct. Mater.* **2006**, *16*, 1488–1498; b) M. Epifani, J. Arbiol, T. Andreu, J. R. Morante, *Eur. J. Inorg. Chem.* **2008**, 859–862; c) M. Epifani, E. Pellicer, J. Arbiol, J. R. Morante, *Chem. Mater.* **2009**, *21*, 862–870; d) M. Epifani, J. Arbiol, T. Andreu, J. R. Morante, *Cryst. Growth Des.* **2010**, *10*, 5176–5181.

[16] $x = 0$: 34-0394; $x = 0.25$: 28-271; $x = 0.4$: 38-1439; $x = 1$: 49-1642.

[17] T. Hirata, H. Zhu, T. Furubayashi, I. Nakatani, *J. Am. Ceram. Soc.* **1993**, *76*, 1361–1364.

[18] V. G. Keramidas, W. B. White, *J. Phys. Chem* **1973**, *59*, 1561–1562.

[19] a) J. E. Spanier, R. D. Robinson, F. Zhang, S. W. Chan, I. P. Herman, *Phys. Rev. B* **2001**, *64*, 245407/1–8; b) F. Zhang, S.-W. Chan, J. E. Spanier, E. Apak, Q. Jin, R. D. Robinson, I. P. Herman, *Appl. Phys. Lett.* **2001**, *80*, 127–129; c) Z. D. Dohcevic-Mitrovic, M. J. Scepanovic, M. U. Grujic-Brojcin, Z. V. Popovic, S. B. Boskovic, B. M. Matovic, M. V. Zinkevich, F. Aldinger, *Solid State Commun.* **2006**, *137*, 387–390.

[20] J. R. McBride, K. C. Hass, B. D. Poindexter, W. H. Weber, *J. Appl. Phys.* **1994**, *76*, 2435–2441.

[21] M. P. Finnegan, H. Zhang, J. F. Banfield, *J. Phys. Chem. C* **2007**, *111*, 1962–1968.

[22] J. Rodriguez-Carvajal, *Physica B* **1993**, *192*, 55–69.

[23] B. Reddy, A. Khan, *Catal. Surv. Asia* **2005**, *9*, 155–171.